Use of a distribution function of relaxation times (DFRT) in impedance analysis of SOFC electrodes

Bernard A. Boukamp[a,*], Aurélie Rolle[b,c]

[a] University of Twente, Fac. of Science and Technology, MESA + Institute for Nanotechnology, P.O. Box 217, 7500 AE Enschede, The Netherlands
[b] Univ. Lille Nord de France, F-59000 Lille, France
[c] CNRS UMR8181, Unité de Catalyse et Chimie du Solide, UCCS, ENSCL, Université Lille 1, F-59652 Villeneuve d'Ascq, France

A B S T R A C T

Electrochemical Impedance Spectroscopy (EIS) is a frequently used method to characterize electrodes for Solid Oxide Fuel Cells (SOFC) or Electrolyzer Cells (SOEC). The porous microstructures, use of composite structures and sometimes extra functional layers in an electrode, result often in impedance spectra that are difficult to analyze. Transformation of the impedance into a distribution function of relaxation times (DFRT) is about to become a new standard in EIS analysis.

This inversion to the τ-domain requires solving a Fredholm integral of the second kind, which is known as an 'ill-posed inverse problem'. Hence the resulting DFRT's should not be trusted directly. In cases were impedance data can be modelled satisfactory with an Equivalent Circuit (EqC), built of known dispersion relations (e.g. (RQ), Gerischer, Finite Length Warburg) an analytic distribution function, $G(\tau)$, can be constructed. This can be compared with the inversion results obtained from Fourier Transform (FT), Tikhonov Regularization (TR) and multi-(RQ) CNLS fits (m(RQ)fit), thus allowing evaluation and validation of these methods This is illustrated in this contribution with four examples of SOFC cathodes with quite different properties. The results apply equally well to SOFC anodes (or SOEC cathodes).

1. Introduction

Solid Oxide Fuel Cell (SOFC) electrodes have a complex microstructure which strongly influences the impedance response. Grainsize, porosity, surface morphology of the grains and the interface between the electrode and electrolyte or barrier layer contribute to the impedance through ionic and electronic transport and diffusion, surface exchange and/or diffusion and bulk redox processes due to the induced variation in the oxygen activity. Especially for composite electrodes the synergy between the two phases [1] is an extra feature complicating interpretation of the impedance spectra. Analysis of the electrode dispersions is not a simple task, model equivalent circuits (EqC's) must be seen as a global approximation of the electrochemical transport and transfer processes. A more fundamental approach is creating an accurate microstructure model through Focussed Ion Beam (FIB) sectioning of the electrode and taking sequential Scanning Electron Micoscope (SEM) images. Using Finite Element Modelling (FEM) with optimized materials parameters, such as diffusion constants, electronic and ionic conductivities and oxygen exchange rates, a model impedance can be simulated and compared with the actual measured dispersion. In a 2006 publication in Nature Materials, Wilson et al. [2] showed the power of

this technique on a YSZ/Ni cermet anode (yttria stabilized zirconia/Ni). A very good match between measured and FIB-FEM modelled electrode dispersion was found. Almar et al. [3] studied the $Ba_{0.5}Sr_{0.5}Co_{0.8}Fe_{0.2}O$ (BSCF) and $La_{0.58}Sr_{0.4}Co_{0.2}Fe_{0.8}O_{3-\delta}$ (LSCF) cathodes with FIB-FEM modelling and impedance analysis. Timurkutluk and Mat have recently presented a review on this method [4].

Unfortunately, the method is rather time consuming and costly. Hence it is not well-suited for 'every day' electrode characterisation procedures. A recent development in the analysis of Electrochemical Impedance Spectroscopy (EIS) is the transformation of the data from the frequency domain (impedance representation) to the τ-domain resulting in a 'Distribution (Function) of Relaxation Times', or DFRT. The DFRT presents the data as a set of peaks, on a $\log(\tau)$ axis, which are characteristic for specific processes that contribute to the electrode impedance. The advantage is that this representation, $G(\tau)$, is 'model-free', i.e. unbiased by a defined model. The data inversion requires solving a Fredholm integral of the second kind:

$$Z(\omega_i) = R_\infty + R_p \int_{-\infty}^{\infty} \frac{G(\tau)}{1 + j\omega_i \tau} \, d\ln\tau \tag{1}$$

with $Z(\omega_i)$ the data set, R_∞ the high frequency cut-off resistance, R_p the

polarization resistance or overall resistance of the dispersion. $G(\tau)$ is a normalized function with $\int_{-\infty}^{\infty} G(\tau)\,d\ln\tau = 1$. The time constant, τ, is the inverse of the frequency: $\tau = (2\pi f)^{-1} = \omega^{-1}$. Solving Eq. (1) is known as an 'ill-posed inverse problem', i.e. there are in principle many solutions possible for $G(\tau)$. The requirement that $G(\tau)$ is always positive puts a serious restriction on the number of possibilities. Several techniques have been developed to invert impedance data to a DFRT: Fourier Transform (FT) [5–8], Tikhonov Regularization (TR) [9–19], Maximum Entropy (ME) [20,21]. All these methods require adjustment of a special parameter in order to get an acceptable DFRT. The FT needs a 'window function' for the inverse transform, generally a 'Hann window' is used which is based on a cosine function [5]. In the Fourier Transform used here a special hyperbolic tangent based function is used [7,8]: TanH(α,β), where α controls the width and β the steepness of the window sides (see ref. [7] for more details). The TR method needs the adjustment of a Regularization Parameter (*RP*). A large *RP* leads to a smooth curve with the danger of losing details, while a small *RP* results in unwanted oscillations in the DFRT. The ME also requires the adjustment of a smoothing parameter.

A different approach has been presented by the current authors with the multi-(RQ) CNLS fit (abbreviated: *m*(RQ)fit [7,8,22]). In this method impedance data is modelled with an increasing number of (RQ) circuits in series, until an acceptable fit is obtained. (RQ) stands for the parallel combination of a resistance, R, and a constant phase element (CPE, symbol Q, with $Y_{(RQ)} = Y_0(j\omega)^\phi$) [23]. The (RQ) is also known as the ZARC element [24]. The advantage is that each (RQ) has an analytical representation in the τ-domain (see Section 2). Hence, when the impedance data can be resolved satisfactory with a series of (RQ)'s, the $R_p \cdot G(\tau)$ is simply obtained by the summation of the respective $R_k \cdot G_k(\tau)$ contributions [22]. Although this approach seems like applying a predefined model, the important criterion is how closely the *m*(RQ)fit matches the actual measurement data. If the difference is in the order of the noise in the data, the *m*(RQ)fit based $R_p \cdot G(\tau)$ is a proper representation, as inserting this back in the integral of Eq. (1) directly results in a close reconstruction of the data set.

A quite different technique is used by the group of Tsur [25–27]. They use an evolutionary programming technique in which a DFRT is built from a pre-determined set of possible distribution functions. A model impedance is reconstructed from the DFRT and compared to the actual measurement. Automatically adjusting the number and type of functions and their parameters through genetic coding, the optimum match is found. The advantage is that no smoothing parameter or window function is needed. It is, however, essential that a physical interpretation can be given to the obtained set of distribution functions.

Besides the (RQ), a few other impedance functions have an analytic τ-domain expression. In principle it is possible to derive the DFRT, $G(\tau)$, directly from the imaginary part of the impedance function, using the method presented by Fuoss and Kirkwood [28]:

$$Z_0 \cdot G(\tau) = \frac{1}{\pi}\left[Z_{imag}\left(z + j\frac{\pi}{2}\right) + Z_{imag}\left(z - j\frac{\pi}{2}\right) \right] \qquad (2)$$

where z is a new variable defined as: $z = \ln(\omega \cdot \tau_0) = \ln(\tau_0/\tau)$. Z_0 is the dc-resistance and τ_0 is the characteristic time constant of the impedance function.

The aim of this publication is to provide a brief review of known exact DFRT's for specific impedance dispersions (Section 2). In cases where the impedance can be well-modelled with an 'Equivalent Circuit' (EqC), which contains one (or more) of these special functions, the analytic DFRT can be calculated and compared with the DFRT's obtained with various inversion techniques (notably the FT, TR and *m*(RQ)fit). This will be illustrated with a number of real examples of electrode materials in the subsequent Sections 3–6. Not only the proper reproduction of the major time constants will be considered but also how-well the reconstructed impedances match the original data sets. This comparison will increase our insight in the application and limitations of the inversion procedures.

2. Exact transforms

2.1. The (RQ) or ZARC

There are quite a few impedance functions that have an analytical τ-domain expression. The best known is the parallel combination of a resistance and a so-called Constant Phase Element or CPE with notation (RQ). Here the circuit description code, as explained in ref. [29], is used. The dispersion is a depressed semi-circle in the impedance representation. The admittance expression for the CPE is:

$$Y_Q(\omega) = Y_0 \cdot (j\omega)^\phi \qquad (3)$$

Hence the impedance expression for a (RQ), ZARC [24] or Cole-Cole relation [30] can be written as:

$$Z_{(RQ)}(\omega) = R\frac{\left(1 + RY_0\omega^\phi\cos\frac{\phi\pi}{2}\right) - jRY_0\omega^\phi\sin\frac{\phi\pi}{2}}{1 + R^2Y_0^2\omega^{2\phi} + 2RY_0\omega^\phi\cos\frac{\phi\pi}{2}}$$

$$= R\frac{\left(1 + (\omega\tau_0)^\phi\cos\frac{\phi\pi}{2}\right) - j(\omega\tau_0)^\phi\sin\frac{\phi\pi}{2}}{1 + (\omega\tau_0)^{2\phi} + 2(\omega\tau_0)^\phi\cos\frac{\phi\pi}{2}} \qquad (4)$$

With the characteristic time constant, $\tau_0 = \sqrt[\phi]{R \cdot Y_0}$. Applying the transformation procedure of Eq. (2) yields the well-known DFRT for the (RQ) dispersion [31]:

$$R \cdot G_{(RQ)}(\tau) = \frac{R}{2\pi} \cdot \frac{\sin(\phi\pi)}{\cosh[\phi\ln(\tau_0/\tau)] + \cos(\phi\pi)} \qquad (5)$$

This results in a symmetric function on a $\ln(\tau)$ scale. The surface area under the $R \cdot G(\tau) - \ln(\tau)$ curve is equal to R. The width of the distribution function strongly depends on φ, as can be seen in Fig. 1. The insert shows the dependence of the full width at half maximum (FWHM, given in decades). When $\varphi = 0.5$, i.e. a diffusion type dispersion, the DFRT extends over a large range. The 10% limit covers 5.2 decades!

For $\varphi = 1$ the CPE becomes a capacitance. The DFRT of a (RC) is a δ-function, i.e. a vertical spike at $\tau_0 = R \cdot C$. The surface area of $R \cdot G_{(RC)}(\tau)$ is not directly accessible from the graph, although mathematically it still equals R. In order to make the contribution of a (RC) better visible in the DFRT graph a Gauss function is applied as distribution function [7,8]:

$$R \cdot G_{(RC)} \approx \frac{R}{W\sqrt{\pi}} e^{-(\ln(\tau_0/\tau)/W)^2} \qquad (6)$$
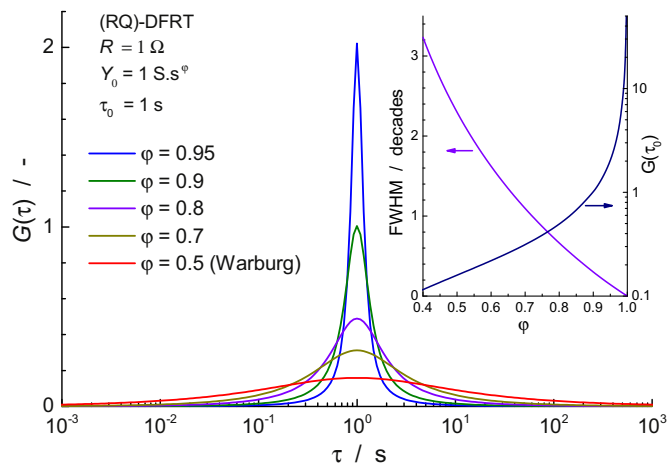

Fig. 1. Distribution functions for a (RQ) or ZARC as function of the frequency power, φ. The insert shows the relation between φ and the full width at half maximum (FWHM in decades) and the maximum $G(\tau_0)$.

The width (and height) is determined by the parameter W. With $W = 0.15$ an acceptable representation of a (RC)-circuit is obtained, while the reconstruction of the impedance from the DFRT shows only a small deviation from the original dispersion. The overall distribution function of a series of (RQ) and/or (RC) circuits is simply obtained by addition of the separate DFRT's:

$$R_p \cdot G(\tau) = \sum_k R_k \cdot G_k(\tau) \tag{7}$$

R_p is the polarization resistance or overall (dc-) resistance of the total frequency dispersion.

2.2. Havriliak-Negami dispersion

The Havriliak Negami dispersion relation [32] is presented in the impedance representation by:

$$Z_{HN}(\omega) = \frac{R_0}{[1 + (j\omega\tau_0)^\beta]^\gamma} \tag{8}$$

This is a very general dispersion relation, for $\gamma = 1$ the CPE or ZARC relation is obtained. With $\beta = 1$ the Cole-Davidson expression results [33]. A special case is the Gerischer [34] or chemical impedance [35,36] which results for $\gamma = 0.5$ and $\beta = 1$:

$$Z_G(\omega) = \frac{R_0}{\sqrt{1 + j\omega\tau_0}} = \frac{R_0}{\sqrt{2}}\left[\sqrt{\frac{\sqrt{1 + \omega^2\tau_0^2} + 1}{1 + \omega^2\tau_0^2}} - j\sqrt{\frac{\sqrt{1 + \omega^2\tau_0^2} - 1}{1 + \omega^2\tau_0^2}}\right] \tag{9}$$

The full expression for the Havriliak-Negami dispersion is:

$$Z(\omega) = \frac{R_0}{\left[1 + \cos\left(\frac{\beta\pi}{2}\right)(\omega\tau_0)^\beta + j\sin\left(\frac{\beta\pi}{2}\right)(\omega\tau_0)^\beta\right]^\gamma} = \frac{R_0}{(a + jb)^\gamma} \tag{10}$$

With: $a = 1 + \cos\left(\frac{\beta\pi}{2}\right)(\omega\tau_0)^\beta$ and $b = \sin\left(\frac{\beta\pi}{2}\right)(\omega\tau_0)^\beta$. The term $(a + jb)^\gamma$ in Eq. (10) can be expanded to:

$$(a + jb)^\gamma = \left\{\cos\left[\gamma\cdot\text{atan}\left(\frac{b}{a}\right)\right] + j\sin\left[\gamma\cdot\text{atan}\left(\frac{b}{a}\right)\right]\right\}(a^2 + b^2)^{\gamma/2} \tag{11}$$

Simulation of the H-N dispersion in a spread sheet is quite straightforward with Eqs. (10), (11).

Several authors have presented an analytic expression for the τ-domain representation of the H-N dispersion [17,37–39]. Here the expression by Bello et al. [38,39], corrected with the missing $(\tau/\tau_0)^{\beta\gamma}$ term, is used:

$$R_0 \cdot G_{HN}(\tau) = \frac{R_0}{\pi}\left(\frac{\tau}{\tau_0}\right)^{\beta\gamma}\frac{\sin(\gamma\theta)}{\left[1 + 2\cos(\pi\beta)\left(\frac{\tau}{\tau_0}\right)^\beta + \left(\frac{\tau}{\tau_0}\right)^{2\beta}\right]^{\gamma/2}} \tag{12a}$$

with: $\theta = \frac{\pi}{2} - \text{atan}\left(\frac{\left(\frac{\tau}{\tau_0}\right)^\beta + \cos(\pi\beta)}{\sin(\pi\beta)}\right) \tag{12b}$

Depending on the parameters β and γ a more or less asymmetric peak is obtained. Fig. 2 shows the change of the DFRT for $\gamma = 0.5$ and β increasing from 0.9 to 1 (resulting in a Gerischer DFRT). The peak maximum is strongly dependent on β, rapidly going to infinity for $\beta \to 1$.

2.3. Gerischer dispersion

Inserting $\beta = 1$ in Eq. (12b) yields '$-\infty$' for the argument of the arctangent function, or atan$(-\infty) = -\frac{1}{2}\pi$, hence $\theta = \pi$. Inserting this in Eq. (12a) directly yields the DFRT for the Gerischer, Eq. (9):
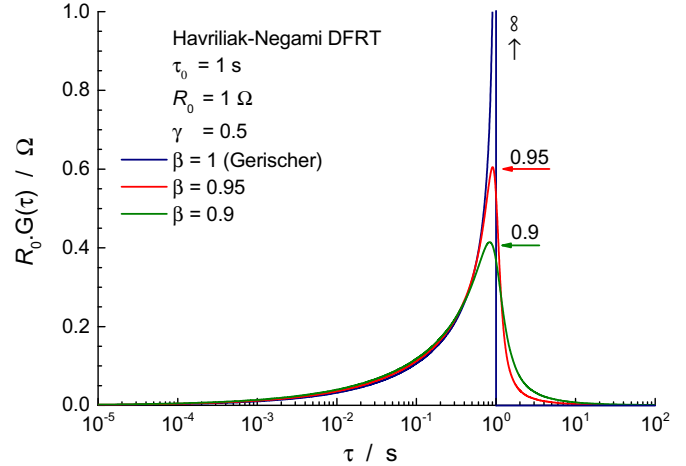
Fig. 2. Three DFRT's for the Havriliak-Negami dispersion, Eqs. (10), (11), as function of the β-parameter with $\gamma = 0.5$. For $\beta = 1$ the asymptotic Gerischer DFRT is obtained.

$$R_0 \cdot G_G(\tau) = \frac{R_0}{\pi}\sqrt{\frac{\tau}{\tau_0 - \tau}}, \tau \le \tau_0 \wedge R_0 \cdot G_G(\tau) = 0, \tau > \tau_0 \tag{13}$$

Fig. 2 clearly shows the asymptotic behaviour at $\tau = \tau_0$.

2.4. Finite Length Warburg

The Finite Length Warburg dispersion (FLW) has a shape that resembles the Gerischer impedance. The significant difference is that the FLW is based on a finite length diffusion problem, while the Gerischer is based on semi-infinite diffusion coupled to a side reaction [34]. Because of this side reaction the Gerischer shows a finite dc-resistance. The short notation for the FLW, with R_0 the dc-resistance, is given by:

$$Z_{FLW}(\omega) = \frac{R_0}{\sqrt{j\omega\tau_0}}\tanh\sqrt{j\omega\tau_0} \tag{14}$$

It is not feasible to derive the DFRT for a FLW using Eq. (2) [22]. As an intermediate step the *fractal*-FLW [40] is explored first. The impedance expression for the *f*-FLW is given by:

$$Z_{f\cdot\text{FLW}}(\omega) = \frac{R_0}{(j\omega\tau_0)^\phi}\tanh(j\omega\tau_0)^\phi, \phi \le 0.5 \tag{15}$$

The full expression with separate real and imaginary parts becomes:

$$Z_{f\cdot\text{FLW}}(\omega) = \frac{R_0}{(\omega\tau_0)^\phi}\cdot\frac{C\cdot\sinh 2\alpha + S\cdot\sin 2\beta - j(S\cdot\sinh 2\alpha - C\cdot\sin 2\beta)}{\cosh 2\alpha + \cos 2\beta} \tag{16}$$

With $C = \cos(\phi\pi/2)$, $S = \sin(\phi\pi/2)$, $\alpha = (\omega\tau_0)^\phi C$ and $\beta = (\omega\tau_0)^\phi S$. Eq. (16) reduces for $\varphi = 0.5$ to the expression for the ideal FLW:

$$Z_{FLW}(\omega) = \frac{R_0}{\sqrt{2\omega\tau_0}}\cdot\left[\frac{\sinh\sqrt{2\omega\tau_0} + \sin\sqrt{2\omega\tau_0}}{\cosh\sqrt{2\omega\tau_0} + \cos\sqrt{2\omega\tau_0}}\right.$$
$$\left. - j\frac{\sinh\sqrt{2\omega\tau_0} - \sin\sqrt{2\omega\tau_0}}{\cosh\sqrt{2\omega\tau_0} + \cos\sqrt{2\omega\tau_0}}\right] \tag{17}$$

Very recently a full analysis has been presented of the transformation of Eq. (16), using the procedure of Eq. (2), into the DFRT for a *f*-FLW [22]:

$$R_0 \cdot G(\tau) = \frac{R_0}{\pi Q}\cdot\frac{\sin(\phi\pi)(1 - Y^2) - 2\cos(\phi\pi)\cdot Y\cdot\sin(2Q\sin(\phi\pi))}{1 + 2Y\cdot\cos(2Q\sin(\phi\pi)) + Y^2} \tag{18}$$

With $Q = (\tau_0/\tau)^\phi$ and $Y = \exp[-2Q\cos(\phi\pi)]$. The DFRT shows several peaks, the number of peaks strongly depends on φ. When φ approaches 0.5 the number of peaks increases very rapidly, see Fig. 3. A remarkable point is that the time constant associated with the major

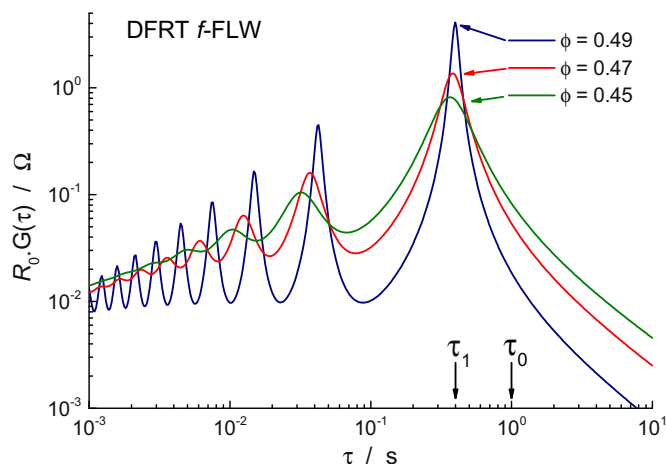**Fig. 3.** Three DFRT's for the *f*-FLW, Eq. (18), with φ = 0.45, 0.47 and 0.49. The time constant of the first peak for φ = 0.49, τ_1, is indicated together with the characteristic time constant, τ_0.

peak, τ_1 (see Fig. 3), lies below the characteristic time constant, τ_0.

In ref. [22] it is shown how the DFRT curve of Eq. (18) changes in to an infinite set of δ-functions when φ → 0.5. The positions, τ_k, of these δ-functions are given by:

$$\tau_k = \frac{\tau_0}{\pi^2 \cdot (k - 0.5)^2}, \quad k = 1, 2, \ldots \tag{19}$$

The mathematical surface area of the δ-functions is given by $R_k = 2\tau_k \cdot R_0$, hence the δ-functions decrease monotonically with τ_k. A δ-function in the τ-domain represents a (RC) impedance. Hence the ideal FLW can also be represented by an infinite series of (RC)-circuits (ref. [22]):

$$Z_{FLW}(\omega) = R_0 \sum_{k=1}^{\infty} 2\tau_k \frac{1 - j\omega\tau_k}{1 + \omega^2\tau_k^2} \tag{20}$$

Fig. 4 shows schematically the DFRT for the ideal FLW, the height of the δ-functions indicate the mathematical surface areas, which is equal to R_k.

3. Havriliak-Negami DFRT

The first example deals with the impedance of a pure $Ca_3Co_4O_{9 + \delta}$ (CCO) cathode in a symmetric cell with a $Ce_{0.9}Gd_{0.1}O_{2.95}$ (CGO)
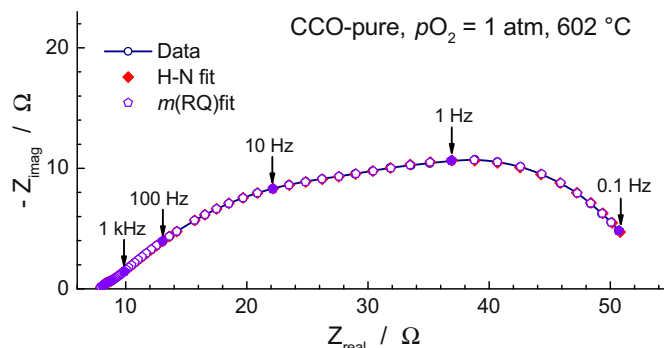
Fig. 5. Impedance diagram for the symmetric CCO sample in oxygen at 602 °C. The CNLS results for the *m*(RQ)fit with four (RQ)'s and the simulation with a Havriliak-Negami dispersion are also shown.

electrolyte, similar to results presented in [41]. The SEM micrographs showed a somewhat flaky and inhomogeneous structure. Fig. 5 shows the impedance, at 602 °C and $pO_2 = 1$ atm, after subtraction of the inductive contribution which is caused by the measurement system. The data point close to 50 Hz was clearly an outlier and was removed from the data set. The overall impedance does not show clear features and cannot be modelled with a simple combination of a few (RQ)'s and/or a Gerischer impedance. A Gerischer impedance could be expected based on prior results obtained for composite CCO-CGO cathodes [1]. Three transformation techniques were used to obtain a DFRT: FT, TR and *m*(RQ)fit. The Fourier Transform method has been described in refs [7,8]. For the Tikhonov Regularization the freely available Matlab app 'DRTtools' was used [42]. 'EqCWin95' software [43] was used for the CNLS-fit in the *m*(RQ)fit procedure. The *m*(RQ)fit [7,8] yielded a R-4(RQ) circuit with $\chi^2 = 4.4 \cdot 10^{-7}$, indicating an excellent fit, as can also be seen in Fig. 5. In the *m*(RQ)fit the used EqC is presented as R-*x*(RQ)*y*(RC), where *x* and *y* indicate the number of (RQ)'s and (RC)'s in the EqC [22]. In the CNLS-fit the φ parameter of the CPE is sometimes shifted to 1, which indicates a (RC) circuit. The error estimates of the (RQ) parameters were in the range from ~2% to ~40%, indicating a strong correlation. The DFRT is characterized by a sharp peak at ~0.3 s, followed by a broad and lower peak as shown in Fig. 6.

Extension of the data set with a R(RQ) circuit at low and at high frequency allowed for a numerical Fourier Transform with analytical extension to $-\infty$ and $+\infty$ in ln(ω) [7,8]. The special Tanh(α,β) window function, with α = 3 and β = 1.5 [7], was used in the reverse Fourier Transform. This resulted in two less sharp peaks, see Fig. 6.

The Tikhonov Regularization (TR, $RP = 10^{-3}$) of the data set showed a rather strange dip at about $2 \cdot 10^{-2}$ s. This could be attributed
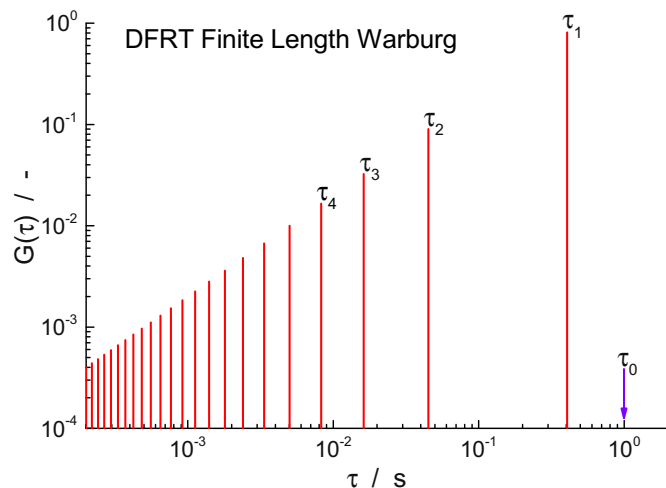

Fig. 4. DFRT for an ideal FLW, Eq. (19). The height of the δ-functions represents the mathematical surface area, $R_k = 2\tau k \cdot R_0$.
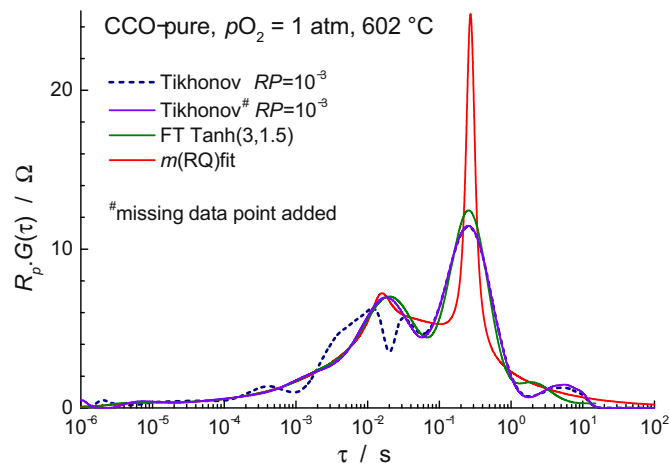

Fig. 6. DFRT for three transform methods for the impedance of Fig. 5. The dashed line represents the TR distribution with the outlier at 50.1 Hz removed (see text).
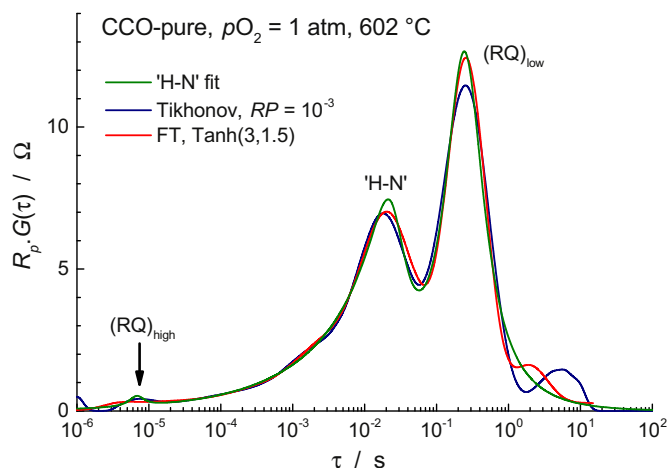
Fig. 7. Comparison of the FT and TR DFRT's with the analytic DFRT for the CNLS analysis with a Havriliak-Negami element.

to the missing data point at $f = 50.1$ Hz in the logarithmically spaced frequency set. Inserting the simulated impedance at 50.1 Hz from the m(RQ)fit alleviated this problem as can also be seen in Fig. 6. Both the FT and the TR curves are quite close to each other.

In [8] it was shown that, depending on the shape, a Havriliak-Negami impedance dispersion could be easily modelled with a series of (RQ)'s, using the m(RQ)fit method. The Gerischer represents an ideal dispersion function, but for porous, inhomogeneous electrodes it might well be replaced by a fractal form, i.e. by a H-N dispersion. This has been observed previously for chromate-titanate based anodes [44]. Using an Excel spread sheet program a quite reasonable fit ($\chi^2 = 1.6 \cdot 10^{-6}$) was obtained for a R(RQ)$_{high}$[H-N](RQ)$_{low}$ circuit, where 'high' and 'low' indicate the position in the frequency range. The simulated dispersion, presented also in Fig. 5, shows an excellent match with the original data. Using the DFRT expressions for the (RQ)'s and the H-N, Eqs. (5), (12a), (12b) the DFRT can be directly obtained. Fig. 7 shows that the H-N based DFRT is a close match to the FT and TR DFRT's.

Fig. 8 shows the relative residuals for the Kramers-Kronig test (data validation) [45], the m(RQ)fit, the H-N based EqC fit and the residuals for the impedances reconstructed from the FT and TR DFRT's. The 'pseudo' χ^2 values indicate high quality data and excellent fits for the CNLS-procedures. The FT reconstructed impedance shows some systematic deviation, while the TR shows a quite acceptable fit. The Fourier Transform and the Tikhonov Regularization show in this
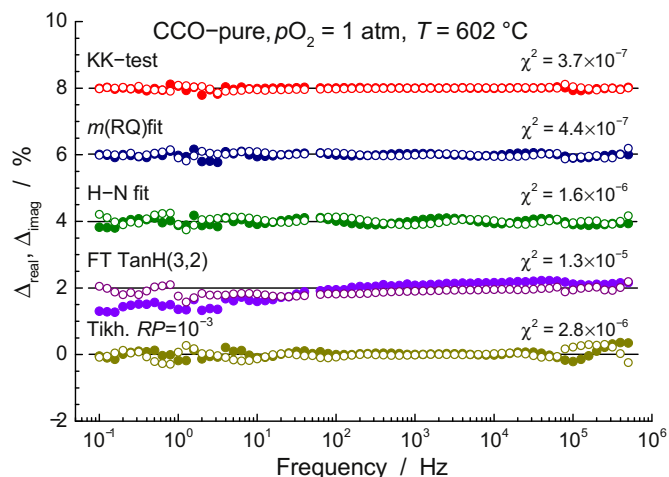

Fig. 8. Relative residuals for the reconstructed impedances. Closed symbols: Δ_{real}, open symbols: Δ_{imag}. The data have been offset by steps of 2%.
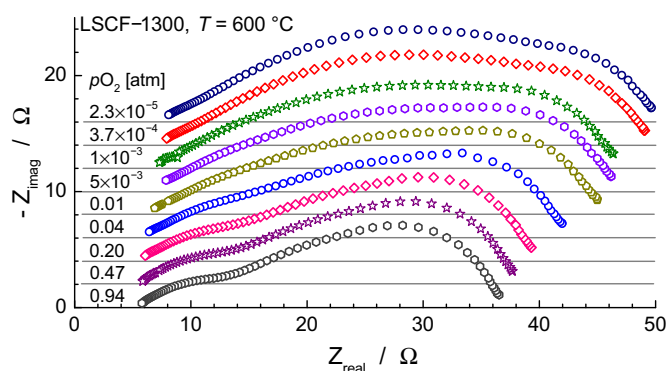

Fig. 9. Impedance diagrams of a symmetric LSCF cathode on CGO as function of pO$_2$ at 600 °C. The diagrams are shifted vertically by steps of 2 Ω for better visibility.

example clearly a good representation, assuming that the electrode shows a fractal-Gerischer behaviour. The asymmetric shape of the smaller peak at $\tau = 0.02$ s can be taken as an indication for a H-N type dispersion [8], although the observation is complicated by the larger peak in Fig. 7.

This example clearly favours the TR and FT techniques. The m(RQ) fit method overestimates the major contribution to the DFRT. The interpretation with a 'fractal-Gerischer' does make sense, but further analysis as function of temperature and/or pO$_2$ should provide further support for this model.

4. La$_{0.6}$Sr$_{0.4}$Co$_{0.2}$Fe$_{0.8}$O$_{3-\delta}$ cathode

The LSCF cathode has been subject of many studies [46]. The cathode properties strongly depend on the microstructure of the electrode, and hence on the sintering temperature, T_s. Too low a T_s causes poor adhesion to the electrolyte resulting in an increase in the polarization resistance, R_p. Too high a T_s causes increased sintering, resulting in a more or less closed pore structure [47,48]. In that case the electrode polarization is significantly increased with respect to the optimal cathode, showing a broad impedance. Fig. 9 presents the dispersion for a symmetric cell with LSCF cathodes, sintered at 1300 °C [47,48], as function of pO$_2$. In a previous DFRT-based study [7] it was indicated that no simple EqC could be formulated that would satisfactory model the data. A DFRT obtained by the genetic algorithm method [25] for a single data set indicated the presence of two Gauss distributions and a (RQ)-DFRT [7].

In this section the DFRT's obtained by the m(RQ)fit method and the Tikhonov Regularization, TR, procedure are compared. Fig. 10 presents m(RQ)fit derived DFRT's as function of selected pO$_2$ values. For almost all data sets a combination of up to 6 (RQ) and (RC) circuits were needed for a good fit. Both the Kramers-Kronig data validation [45] and the m(RQ)fit results showed (pseudo) χ^2 values well below 10^{-6}, indicating both high quality data and a very good m(RQ)fit.

All m(RQ)fit DFRT's are characterized by a very broad distribution and one sharp peak at low frequencies ($\tau_1 \sim 0.7$ s). This peak, which is a Gauss function representing a (RC) contribution in the m(RQ)fit, is marginally dependent on pO$_2$. The very broad peak, at τ_2, shows a somewhat stronger pO$_2$ dependence. The associated resistances, R_1 and R_2, show a small but clear power dependence on pO$_2$. The orders of the dependence, m, are presented in the insert in Fig. 10. Table 1 summarizes the m(RQ)fit results.

The TR transformations show a quite different picture, see Fig. 11. The time constant, τ_1, also stays more or less constant, the peak at the second time constant, τ_2, is less clear as for the m(RQ)fit method of Fig. 10. At the high frequency side ($\tau < 10^{-4}$ s) cut-off noise is present. Using the EqC for the pO$_2 = 0.94$ atm dispersion a new simulation was made over a frequency range from 0.1 MHz to 6.5 MHz. The TR DFRT is shown in the insert of Fig. 11 together with the original TR-
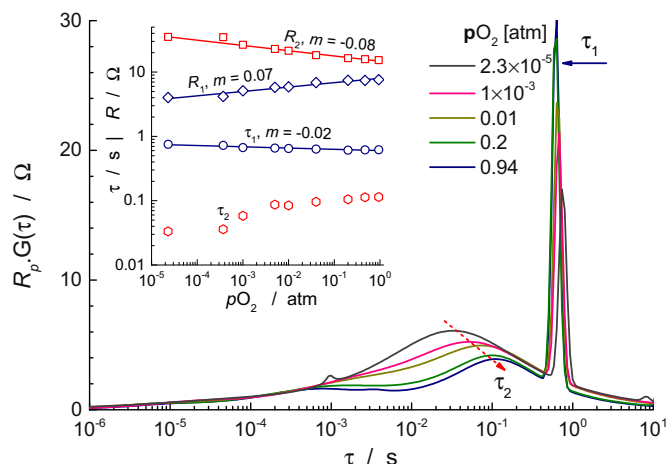
Fig. 10. DFRT obtained by the m(RQ)fit method from the impedance data of Fig. 9. Insert shows the pO$_2$ dependence of the major time constants and the related resistances.

Fig. 12. Temperature dependence of the DFRT obtained with the m(RQ)fit method for the LSCF sample. Insert shows the Arrhenius plot for the two major time constants.

Table 1
Fit results for the LSCF cathode dispersions as function of pO$_2$. The EqC resulting from the m(RQ)fit and the pseudo χ^2 values (CNLS-fit and KK-validation) are presented.

pO$_2$/atm	m(RQ)fit EqC	$\chi_{CNLS}^2 \times 10^6$	$\chi_{KK}^2 \times 10^6$
0.94	4(RQ)2(RC)	0.11	0.15
0.47	3(RQ)3(RC)	0.66	0.28
0.20	4(RQ)2(RC)	0.36	0.24
0.04	4(RQ)2(RC)	0.69	0.68
0.01	4(RQ)2(RC)	0.65	0.46
$5 \cdot 10^{-3}$	3(RQ)3(RC)	0.47	0.65
$1 \cdot 10^{-3}$	3(RQ)2(RC)	0.41	0.14
$3.7 \cdot 10^{-4}$	3(RQ)1(RC)	0.22	0.10
$2.3 \cdot 10^{-5}$	3(RQ)3(RC)	0.28	0.17

Table 2
Fit results for the LSCF cathode dispersions as function of temperature. The EqC resulting from the m(RQ)fit and the pseudo χ^2 values (CNLS-fit and KK-validation) are presented. (Obvious outliers have been removed from the data).

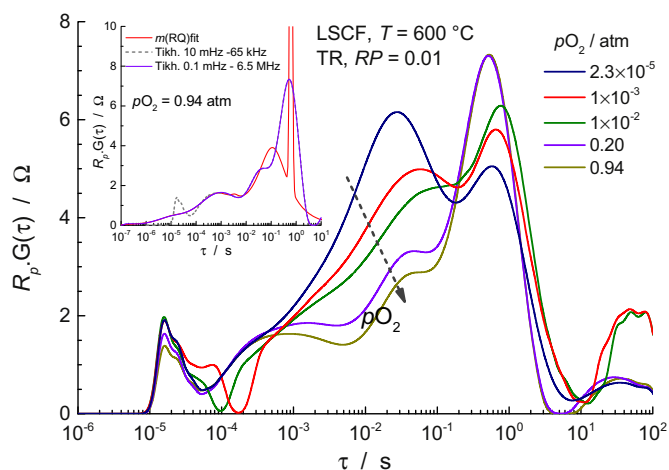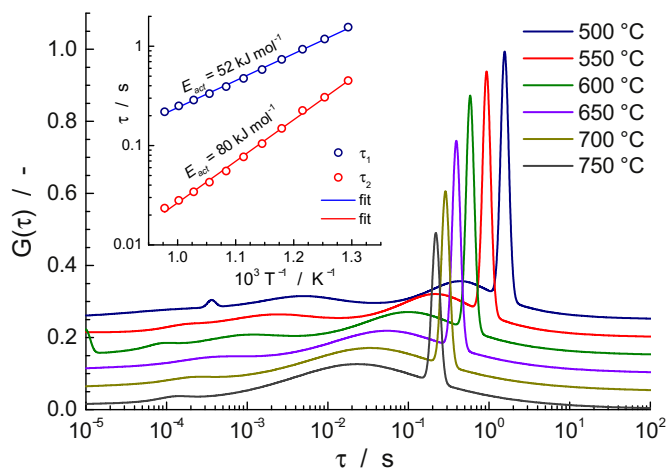| T/°C	m(RQ)fit EqC	$\chi_{CNLS}^2 \times 10^6$	$\chi_{KK}^2 \times 10^6$
500	3(RQ)2(RC)	0.30	0.33
525	3(RQ)2(RC)	1.4	1.9
550	4(RQ)1(RC)	1.2	1.5
575	4(RQ)1(RC)	1.4	2.0
600	3(RQ)2(RC)	0.85	0.1
625	3(RQ)2(RC)	0.61	0.15
650	3(RQ)1(RC)	0.80	0.29
675	3(RQ)1(RC)	0.70	0.23
700	3(RQ)1(RC)	1.1	0.21
725	3(RQ)1(RC)	1.3	0.26
750	3(RQ)1(RC)	1.3	0.19

Fig. 11. TR DFRT's obtained for the data of Fig. 9 with $RP = 0.01$. Selected DFRT's are shown. The insert compares the influence of an extended frequency range with standard TR DFRT and the m(RQ)fit DFRT.
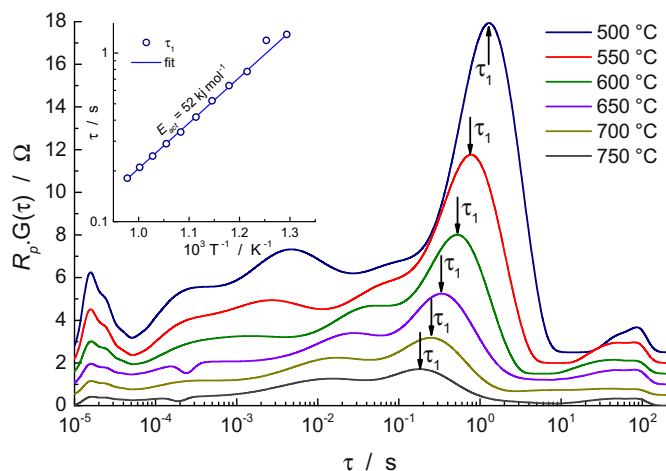

Fig. 13. Temperature dependence of the DFRT obtained with the TR method with $RP = 10^{-3}$. The insert shows the Arrhenius plot for the τ_1.

DFRT and the m(RQ)fit DFRT. At high frequencies ($\tau < 10^{-3}$ s) both the extended TR and the m(RQ)fit DFRT's coincide quite nicely. Above $\tau = 10^{-3}$ s both TR DFRT's coincide very well.

Fig. 12 show the m(RQ)fit derived DFRT's for selected temperatures, fit results are summarized in Table 2. It is again characterized by two major time constants, τ_1 and τ_2, with activation energies of respectively 52 and 80 kJ mol^{-1}. At low temperatures even a third time constant becomes visible. The TR transform clearly shows the major peak, the second broader peak is less well defined, see Fig. 13. The shift of τ_1 with temperature, insert in Fig. 13, shows also an activation energy of

52 kJ mol^{-1}.

This impedance study of the LSCF cathode sintered at 1300 °C was part of a series with different T_s: 1100 °C, 1200 °C and 1300 °C. The polarization resistances have quite different activation energies, resp. 140 kJ mol^{-1}, 120 kJ mol^{-1} and 52 kJ mol^{-1}. This clearly indicates a distinct difference in the dominating electrode processes between the cathodes sintered at 1100 °C and 1200 °C and this electrode. The capacitance associated with τ_1 is 0.27–0.44 F·cm^{-2} ($\sim$170 F·cm^{-3} at
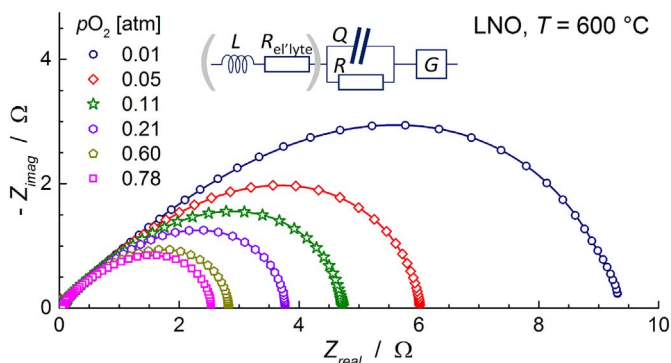
Fig. 14. Impedance diagrams of a symmetric LNO cathode on CGO as function of pO_2 at 600 °C. The applied EqC is presented. The brackets show the inductance and electrolyte resistance that have been subtracted.

750 °C), which is well below the 1135 F·cm^{-3} for the redox capacitance at 750 °C estimated for dense thin films of LSCF [49,50]. Nevertheless this capacitance can be assigned to the redox capacitance of LSCF, assuming that a limited layer thickness of the electrode is active. The associated resistance, with $E_{act} \sim$ 55 kJ mol^{-1} (up to 650 °C), could then be assigned to the lattice transfer of adsorbed oxygen. Unfortunately, in literature there is no reliable data available on the oxygen incorporation step. Even for the overall oxygen exchange rate for LSCF (comprising the dissociation and incorporation steps) conflicting results appear in literature.

5. Electrode dispersion with a Gerischer

An extensive study on the electrode behaviour of La$_2$NiO$_{4+\delta}$ (LNO) cathodes has been presented in ref. [51]. The screen printed LNO cathodes showed a typical EqC consisting of a Gerischer dispersion in series with a (RQ) at high frequencies. Fig. 14 shows the dispersions as function of $pO2$ at 600 °C. The instrumental inductance and electrolyte resistance have been subtracted from the dispersions. The drawn lines show an excellent CNLS-fit of the model EqC with the measured data. The microstructure showed an open porosity with well-defined crystallites with an average grain size of 340 nm.

In this case we can compare the exact EqC-derived DFRT with the m(RQ)fit and TR methods. Fig. 15 shows the combination of these DFRT's at $pO_2 = 0.01$ atm. The Gerischer impedance shows a clear (RC) type dispersion at the low frequency limit [8]. The inversion of a (RC) is problematic because the associated distribution function is a δ-function
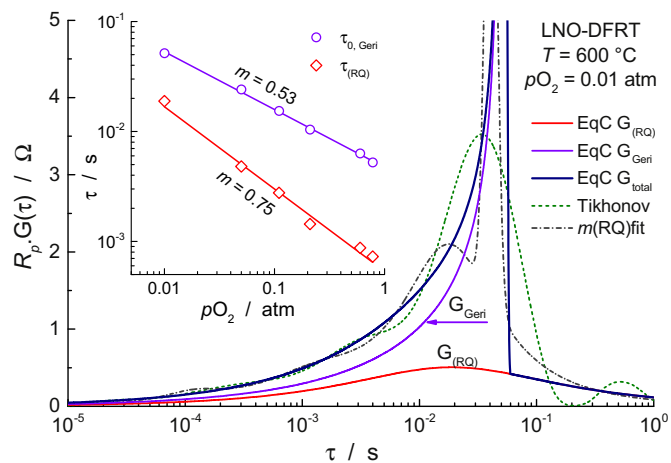
Table 3
Fit results for LNO cathode as function pO_2. Both the m(RQ)fit and the EqC CNLS-fit are presented with the respective pseudo χ^2 values (including the KK-validation).

pO_2/atm	m(RQ)fit EqC	$\chi_{CNLS}^2 \times 10^6$	EqC	$\chi_{CNLS}^2 \times 10^6$	$\chi_{KK}^2 \times 10^6$
0.78	2(RQ) 2(RC)	0.027	LR(RQ)G	0.041	0.033
0.60	2(RQ) 2(RC)	0.030	LR(RQ)G	0.044	0.028
0.21	4(RQ)	0.028	LR(RQ)G	0.066	0.028
0.11	4(RQ)	0.034	LR(RQ)G	0.068	0.034
0.05	4(RQ)	0.025	LR(RQ)G	0.091	0.025
0.01	3(RQ) 1(RC)	0.059	LR(RQ)G(RQ)	0.15	0.059

in the τ-domain [7]. For a pure Gerischer dispersion two peaks are obtained with the m(RQ)fit method as demonstrated in refs [7,8]. The EqC derived DFRT in Fig. 15 is characterized by an asymptotic function (Eq. (13): $G_{Geri}(\tau_0) = \infty$) and a very broad symmetric distribution function, i.e. the inverse of a (RQ). Neither the m(RQ)fit nor the TR inversion can correctly model this behaviour. The m(RQ)fit in Fig. 15 shows two peaks, at τ ∼ 20 ms and τ ∼ 45 ms, which can be assigned to the (RQ) at τ = 20 ms and the Gerischer at τ = 55 ms. The insert shows the two related time constants derived from the CNLS-fit with the EqC (inset in Fig. 14). The CNLS-fit results for the EqC and the m(RQ)fit are summarized in Table 3.

Fig. 16 shows the development of the m(RQ)fit with pO_2. At higher pO_2 (> 0.11 atm) the m(RQ)fit reveals two sharp peaks, besides the broader peak assigned to the (RQ). This has been observed before [7,8]. In the insert the peak positions, τ_1, τ_2 and τ_3, are compared with the actual EqC values (see insert in Fig. 15). The DFRT at higher pressures develop a second sharp peak at τ_2, which has the same pO_2 dependence as the major peak. Hence τ_1 and τ_2 are part of the same distribution function for the Gerischer. The order, m, is somewhat lower than observed for the EqC derived DFRT, see insert in Fig. 16. τ_3 is clearly linked to $\tau_{(RQ)}$.

The Tikhonov and Fourier Transform DFRT show much broader, and almost identical, distribution functions as presented in Fig. 17. The peak positions, τ_1, show the same pO_2 dependence, but are shifted to lower τ values. Further peaks are less well developed and difficult to estimate. In this case the m(RQ)fit method has a small advantage over the TR or FT method as it can resolve most time constants.
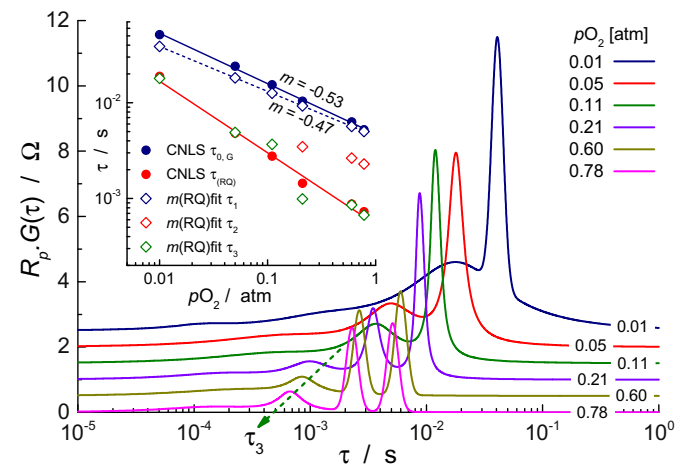

Fig. 15. The analytical distribution function (heavy line) for the LNO electrode at 0.01 atm is presented with its two components. Dashed lines show the TR and m(RQ)fit distribution functions. Insert shows the time constants obtained from the CNLS-fits.

Fig. 16. Presentation of the m(RQ)fit DFRT's. These have been offset by 0.5 Ω for better visibility. The insert shows the three time constants derived from the distribution functions, together with the exact $\tau_{0,G}$ and $\tau_{(RQ)}$.
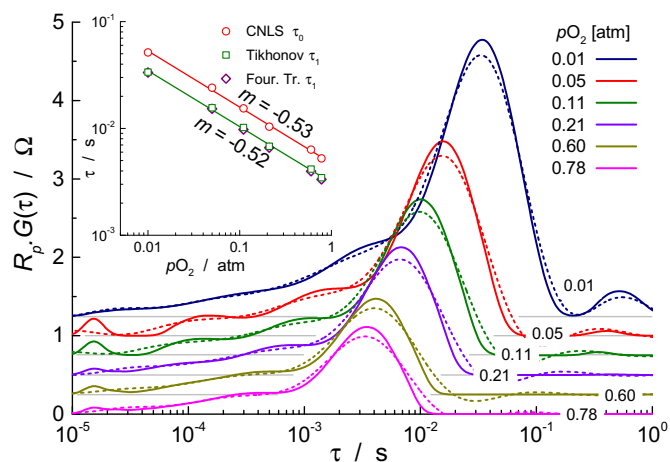
Fig. 17. DFRT's derived from the impedances of Fig. 14. Heavy lines: Tikhonov regularization with $RP = 10^{-3}$. Dashed curves: Fourier Transform following the method of ref. [7] with a TanH window (with: $\alpha = 2.5$, $\beta = 1.5$). Curves have been offset by 0.25 Ω. In the insert the major time constants are compared. Time constants for the TR and FT are almost identical.

6. FLW dispersion

As indicated in the introduction, the microstructure of the electrode has a significant influence on the shape and magnitude of the impedance. Here we consider the impedance of pure CCO deposited by Electrostatic Spray Deposition (ESD) [52]. In contrast to the example in Section 3, this electrode shows a structure with well-defined microcrystals. Details on the preparation procedure and further characterizations will be part of a future publication. Measurements were performed on a symmetric cell with CGO as electrolyte. Fig. 18 shows a compilation of normalized impedances measured at temperatures in the range 600–800 °C. Normalization was done by subtracting the instrumental inductance and electrolyte resistance, followed by dividing the remaining dispersions by the polarization resistances. Almost all impedances (except for the lowest temperatures) show an identical dispersion, characterized by a 45° line at high frequencies, followed by a more or less (RC) type dispersion at low frequencies. It can be regarded as a Finite Length Warburg type dispersion, which is not uncommon for SOFC electrodes.

Fig. 19 shows an impedance at 751 °C which could be fitted by the series combination of two FLW elements (FLW-A and FLW-B). This however is an approximation, it is more likely that the FLW-like
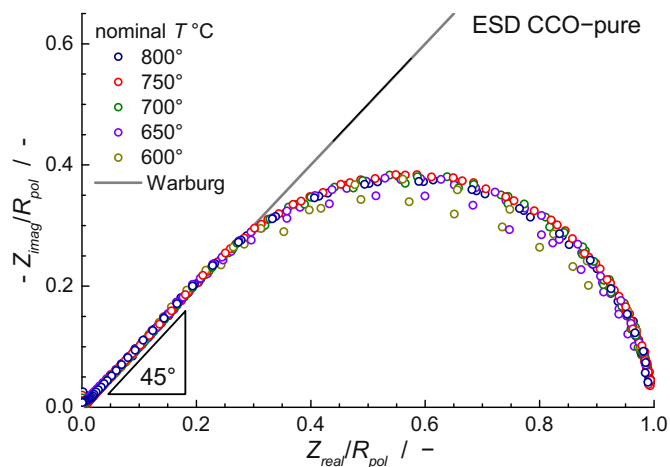

Fig. 19. Impedance of the ESD CCO cathode at 751 °C, together with the two FLW CNLS-fit result. The insert shows the relative error distributions for the m(RQ)fit and the two FLW fit.

dispersion is due to a combination of parallel FLW functions with a distribution in the diffusion length (with $\tau_0 = \ell^2/\widetilde{D}$). The m(RQ)fit resulted in a 2(RQ)2(RC) circuit, which was used for the inversion to a DFRT. The relative errors remained for the most part below 0.2%, indicating a very good fit.

Fig. 20 shows the DFRT's for the dispersion of Fig. 19. The distribution function for the two FLW fit could be directly calculated using Eq. (19). The δ-functions have been replaced for better visibility by Gauss peaks using Eq. (6). The m(RQ)fit shows a reasonable match with the FLW-DFRT with respect to position of the first peaks at τ_1. The TR-DFRT with $RP = 10^{-4}$, shows a rather broad peak overlapping the two FLW-peaks. The peaks below 0.03 s have been enlarged 10 times for better visibility (dashed lines). The FT-DFRT (not shown) is in shape quite similar the TR-DFRT, with an identical peak position.

It is clear that neither the Tikhonov regularization nor the Fourier transform is capable in recognizing the two major peaks related to the two FLW dispersions. On the other hand, a more complex FLW-related function might be possible with a distribution in the diffusion length and hence in the characteristic time constant, τ_0.

7. Discussion

It is clear from the previous Sections 3–6 that different inversion

Fig. 18. Compilation of the normalized impedances for the ESD CCO symmetric sample. The high frequency part follows exactly a Warburg dispersion (45°). Temperatures are ± 5 °C.
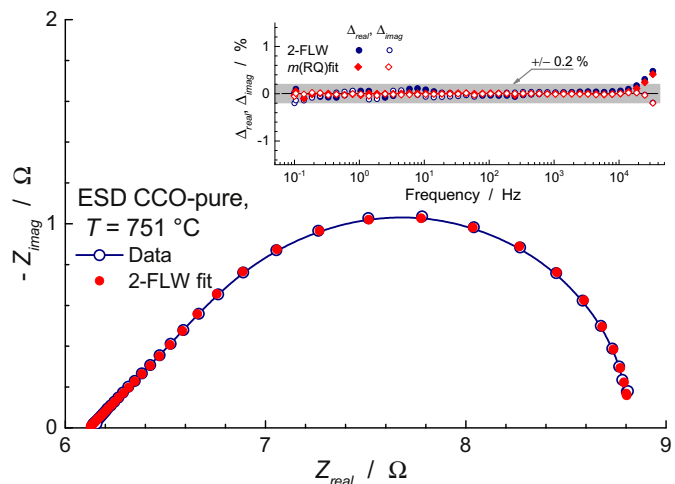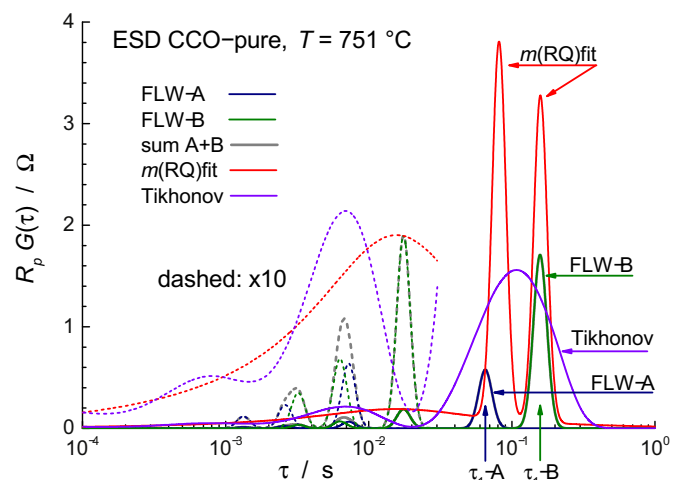

Fig. 20. DFRT's derived for the ESD-CCO sample ($T = 751$ °C). The distribution functions are magnified 10 times below 0.03 s for better visibility.

techniques can lead to quite different shapes of the distribution functions. Yet, the reconstructed impedances show generally a very good match with the original data, see Figs. 8 and 19, and results presented in [7,8,22]. This indicates that different DFRT shapes can properly represent the measured data set in the τ-domain. With the help of a set of exact distribution functions (Section 2) it is possible to present reliable DFRT's for impedance data that can be resolved with a realistic EqC, see e.g. Fig. 15 for the LNO electrode (Section 5). When (RC) type dispersions are present (this includes also the Gerischer and FLW) then the FT and Tikhonov inversion methods show a clear deviation from the exact DFRT. In general both the FT and Tikhonov inversions give quite similar results as shown in Section 3, Fig. 7, and in Section 5, Fig. 17. The m(RQ)fit technique can often resolve the impedance spectra close to the experimental noise level. However, with the Gerischer and the FLW an overestimation of the number of peaks can occur [7,8,22], i.e. the appearance of a 'satellite' peak.

The position of the time constants obtained from a TR or FT inversion can deviate from the exact positions derived from a realistic EqC, see e.g. Fig. 17. The trend (i.e. the order of the pO_2 dependence, m), however, is very close as can be seen in the insert in Fig. 17. It seems that, in the case of the Gerischer type dispersion, the m(RQ)fit derived time constants are quite close to the exact ones, despite the appearance of a satellite peak for the Gerischer, see the insert in Fig. 16.

An important point is, of course, the quality of the data. As shown in Section 3, the Tikhonov Matlab app [42] requires well-spaced data points. Removing an outlier results in a distortion of the DFRT. Replacement of the outlier with an interpolated data point restores the DFRT. Another point is the frequency range which should be as large as possible. With the FT method the frequency range is extended on both sides, but this is not 'model free' as a simple R(RQ) circuit is used for the extension. For the TR method the low frequency limit data point should be close to the dc-point, otherwise a broad hump appears at the high τ limit, as can be seen in Figs. 6 and 11.

Zhang et al. [18] have shown that increasing the number of data sets per decade improves the Tikhonov inversion for a Gerischer type dispersion. But taking 100 data points per decade is for routine use not advisable. In a subsequent publication [19] Zhang et al. have presented a 'high precision approach' Tikhonov based inversion, in which also the errors between the measured impedance and reconstructed impedance are involved. Effat and Ciucci [53] have recently presented an improved inversion method, based on Bayesian regularization, which involves the use of 'prior models'. Hopefully these new methods will become available to the scientific community, as has been done previously by Wan with the 'DRTtools app' [42].

8. Conclusions

The distribution function of relaxation times has become an important tool for electrochemical impedance spectroscopy. It is, however, still a technique that needs to be applied with care. Comparison of the 'exact' distribution function from a viable Equivalent Circuit with the DFRT derived with one of the inversion techniques, as described in this contribution, will help in understanding the limitations. Especially (RC)-type dispersions (including the Gerischer and the FLW) provide poor representations in the τ-domain when using the standard available techniques (TR, FT). The m(RQ)fit has some advantage in this case, as it shows the time constants more accurately than the TR or FT method, but it can also produce 'satellite' peaks for the Gerischer of FLW dispersions. The drawback of the m(RQ)fit is that it is not guaranteed to provide an acceptable fit, sometimes a 'negative' (RQ) is encountered (not presented here). It is to be expected that advanced inversion techniques [19,53] will become available in the near future.

Acknowledgement

References

[1] A. Rolle, H.A.A. Mohamed, D. Huo, E. Capoen, O. Mentré, R.-N. Vannier, S. Daviero-Minaud, B.A. Boukamp, Solid State Ionics 294 (2016) 21–30.
[2] J.R. Wilson, W. Kobsiriphat, R. Mendoza, H.-Y. Chen, J.M. Hiller, D.J. Miller, K. Thornton, P.W. Voorhees, S.B. Adler, S.A. Barnett, Nat. Mater. 5 (2006) 541–544.
[3] L. Almar, J. Szász, A. Weber, E. Ivers-Tiffée, J. Electrochem. Soc. 164 (2017) F289–F297.
[4] B. Timurkutluk, M.D. Mat, Int. J. Hydrog. Energy 41 (2016) 9968–9981.
[5] H. Schichlein, A.C. Müller, M. Voigts, A. Krügel, E. Ivers-Tiffée, J. Appl. Electrochem. 32 (2002) 875–882.
[6] A. Leonide, V. Sonn, A. Weber, E. Ivers-Tiffée, J. Electrochem. Soc. 155 (2008) B36–B41.
[7] B.A. Boukamp, Electrochim. Acta 154 (2015) 35–46.
[8] B.A. Boukamp, A. Rolle, Solid State Ionics 302 (2017) 12–18.
[9] J. Macutkevic, J. Banys, A. Matulis, Nonlinear Anal. Modell. Control 9 (2004) 75–88.
[10] V. Sonn, A. Leonide, E. Ivers-Tiffée, J. Electrochem. Soc. 155 (2008) B675–B679.
[11] J.P. Schmidt, T. Chrobak, M. Ender, J. Illig, D. Klotz, E. Ivers-Tiffée, J. Power Sources 196 (2011) 5342–5348.
[12] H. Sumi, T. Yamaguchi, K. Hamamoto, T. Suzuki, Y. Fujishiro, T. Matsui, K. Eguchi, Electrochim. Acta 67 (2012) 159–165.
[13] J. Illig, J.P. Schmidt, M. Weiss, A. Weber, E. Ivers-Tiffée, J. Power Sources 239 (2013) 670–679.
[14] T. Ramos, M. Søgaard, M.B. Mogensen, J. Electrochem. Soc. 161 (2014) F434–F444.
[15] S. Kazlauskas, A. Kežionis, T. Šalkus, A.F. Orliukas, Solid State Ionics 231 (2013) 37–42.
[16] M. Saccoccio, T.H. Wan, C. Chen, F. Ciucci, Electrochim. Acta 147 (2014) 470–482.
[17] T.H. Wan, M. Saccoccio, C. Chen, F. Ciucci, Electrochim. Acta 184 (2015) 483–499.
[18] Y. Zhang, Y. Chen, M. Yan, F. Chen, J. Power Sources 283 (2015) 464–477.
[19] Y. Zhang, Y. Chen, M. Li, M. Yan, M. Ni, Ch. Xia, J. Power Sources 308 (2016) 1–6.
[20] T. Hörlin, Solid State Ionics 67 (1993) 85–96.
[21] T. Hörlin, Solid State Ionics 107 (1998) 241–253.
[22] B.A. Boukamp, Electrochim. Acta 252 (2017) 154–163.
[23] J.R. Macdonald, Solid State Ionics 13 (1984) 147–149.
[24] E. Barsoukov, J.R. Macdonald (Eds.), Impedance Spectroscopy: Theory, Experiment, and Applications, 2nd edition, John Wiley & Sons, Hoboken, NJ, 2005.
[25] S. Hershkovitz, S. Baltianski, Y. Tsur, Solid State Ionics 188 (2011) 104–109.
[26] Z. Drach, S. Hershkovitz, D. Ferrero, P. Leone, A. Lanzini, M. Santarelli, Y. Tsur, Solid State Ionics 288 (2016) 307–310.
[27] A.K. Baral, Y. Tsur, Solid State Ionics 304 (2017) 145–149.
[28] R.M. Fuoss, J.G. Kirkwood, J. Am. Chem. Soc. 63 (1941) 385–394.
[29] CDC_Explained.pdf, available from: www.utwente.nl/tnw/ims/publication/downloads/.
[30] K.S. Cole, R.H. Cole, J. Chem. Phys. 9 (1941) 341–351.
[31] F. Dion, A. Lasia, J. Electroanal. Chem. 475 (1999) 28–37.
[32] S. Havriliak, S. Negami, Polymer 8 (1967) 161.
[33] D.W. Davidson, R.H. Cole, J. Chem. Phys. 19 (1951) 1484–1490.
[34] B.A. Boukamp, H.J. Bouwmeester, Solid State Ionics 157 (2003) 29–33.
[35] S.B. Adler, J.A. Lane, B.C.H. Steele, J. Electrochem. Soc. 143 (1996) 3554–3564.
[36] Y. Lu, C. Kreller, S.B. Adler, J. Electrochem. Soc. 156 (2009) B513–B525.
[37] F. Alvarez, A. Alegra, J. Colmenero, Phys. Rev. B 44 (1991) 7306–7312.
[38] A. Bello, E. Laredo, M. Grimau, Phys. Rev. B 60 (1999) 12764–12774.
[39] A. Bello, E. Laredo, M. Grimau, J. Chem. Phys. 113 (2000) 863–868.
[40] Z. Stoynov, Electrochim. Acta 35 (1990) 1493–1499.
[41] A. Rolle, V. Thoréton, P. Rozier, E. Capoen, O. Mentré, B. Boukamp, S. Daviero-Minaud, Fuel, Cell 12 (2012) 288–301.
[42] DRT Tools and Manual, https://sites.google.com/site/drttools/.
[43] A. Wisse, B.A. Boukamp, EqCWin95, www.wisseq.nl/portfolio.aspx (in Dutch).
[44] M. Gonzàlez-Cuenca, W. Zipprich, B.A. Boukamp, G. Pudmich, F. Tietz, Fuel Cells 1 (2001) 256–264.
[45] B.A. Boukamp, J. Electrochem. Soc. 142 (1995) 1885–1894.
[46] M.M. Kuklja, E.A. Kotomin, R. Merkle, Yu.A. Mastrikova, J. Maier, Phys. Chem. Chem. Phys. 15 (2013) 5443–5471.
[47] N. Hildenbrand, Thesis, University of Twente, the Netherlands, 2011 (ISBN: 978-94-91211-57-7, Chap. 4).
[48] N. Hildenbrand, B.A. Boukamp, P. Nammensma, D.H.A. Blank, Solid State Ionics 192 (2011) 12–15.
[49] B.A. Boukamp, N. Hildenbrand, P. Nammensma, D.H.A. Blank, Solid State Ionics 192 (2011) 404–408.
[50] B.A. Boukamp, N. Hildenbrand, H.J.M. Bouwmeester, D.H.A. Blank, Solid State Ionics 283 (2015) 81–90.
[51] N. Hildenbrand, P. Nammensma, D.H.A. Blank, H.J.M. Bouwmeester, B.A. Boukamp, J. Power Sources 238 (2013) 442–453.
[52] E. Djurado, A. Salaün, G. Mignardi, A. Rolle, M. Burriel, S. Daviero-Minaud, R.N. Vannier, Solid State Ionics 286 (2016) 102–110.
[53] M.B. Effat, F. Ciucci, Electrochim. Acta 247 (2017) 1117–1129.